RF-waveform optimization for MHz-rate DFB laser absorption spectroscopy in dynamic combustion environments

Anil Nair, Nicolas Minesi, Christopher Jelloian, Nicholas Kuenning, Raymond Spearrin

RF-waveform optimization for MHz-rate DFB laser absorption spectroscopy in dynamic combustion environments

Anil P. Nair*, Nicolas Q. Minesi†, Christopher Jelloian*, Nicholas M. Kuenning‡, and R. Mitchell Spearrin§
University of California, Los Angeles (UCLA), Los Angeles, CA 90095, USA

Methods to extend the spectral tuning range and signal-to-noise ratio via waveform optimization were examined using diplexed RF-modulation with continuous-wave distributed-feedback lasers, with relevance to MHz-rate laser absorption spectroscopy. With a bias-tee circuit, laser chirp rates are shown to increase by modulating the AC input voltage using square waves instead of sine waves and by scanning the laser below the lasing threshold. The effect of square waveform duty cycle and leading edge ramp rate are examined. Scan depths on the order of 1 cm^{-1} at a rate of 1 MHz are achieved with continuous-wave DFB quantum cascade lasers. The attenuation of the high-frequency laser signals due to detector bandwidth are also examined, and limitations are noted. Based on common detection system limitations, an optimization approach is established for a given detection bandwidth, with a representative optimized waveform determined for a 200 MHz system. This waveform is validated for accuracy across the scan range and for scan-to-scan repeatability using room temperature laser absorption measurements. The method is then deployed in a detonation tube to measure temperature, pressure, and CO concentration at MHz rates.

I. Nomenclature

D	=	depth of current modulation
f^*	=	characteristic frequency of spectral feature in detector siganl
f_{BW}	=	detection system bandwidth
H	=	voltage-to-current transfer function
I_{lim}	=	maximum allowable injection current for laser
I_{pp}	=	peak-to-peak amplitude of current waveform applied to laser
I_{set}	=	DC current applied to laser
I_0	=	incident/background light intensity
I_{t}	=	transmitted light intensity
I_{th}	=	laser threshold current
P	=	gas pressure
R	=	chirp rate
T	=	gas temperature
V_{max}	=	maximum value of voltage output by function generator
V_{min}	=	minimum value of voltage output by function generator
V_{pp}	=	peak-to-peak amplitude of voltage signal from function generator
X_{CO}	=	carbon monoxide mole fraction
α	=	absorbance
ν	=	laser output wavenumber
$\Delta\nu$	=	spectral scan depth
$\Delta\nu_{\mathrm{use}}$	=	usable spectral wavenumber scan depth
$\Delta\nu_C$	=	collision line width
τ^*	=	characteristic time for spectral feature in detector signal

*Ph.D. Candidate, Mechanical and Aerospace Engineering Department
†Postdoctoral Scholar, Mechanical and Aerospace Engineering Department
‡Ph.D. Student, Mechanical and Aerospace Engineering Department
§Associate Professor, Mechanical and Aerospace Engineering Department

II. Introduction

High-speed diagnostics are invaluable for the assessment of the highly transient physical processes occuring in detonation engines, which often feature periodic phenomena with temporal frequencies on the order of 10s of kHz. The measurement of time-resolved thermodynamic and thermochemical properties can aid in the improvement of the physical models of these systems and in the diagnosis of performance shortcomings. Laser absorption spectroscopy (LAS) has proven useful in measuring gas properties in detonation environments [1–8], namely temperature and species. Initial near-MHz rate LAS approaches for detonation engines utilized fixed-wavelength laser absorption [7, 9, 10]. However, this approach is generally not robust to beam steering, particle scattering, and thermal emission, which are pronounced in detonation engines, particularly those that are rocket-based, rendering such measurement strategies less than ideal. In recent years, scanned-wavelength LAS techniques have been deployed on detonation engines [11], leveraging additional spectral information to mitigate numerous deleterious effects occurring in harsh environments such as thermal emission, non-absorbing baseline, mechanical vibration, and beam steering. Unfortunately, most scanned-wavelength LAS techniques have been limited to measurement rates on the order of 10–100 kHz, which are insufficient to fully resolve the flow transients between detonation cycles. To address this shortcoming, our group has recently developed a method to extend scanned-wavelength laser absorption spectroscopy to MHz rates and the mid-wave infrared by utilizing diplexed radio-frequency modulation with distributed feedback (DFB) lasers enabled by the usage of a bias-tee circuit [2, 12–15]. We demonstrated this method for measurement of infrared spectral transitions of carbon monoxide and carbon dioxide in a rotating detonation engine using two continuous-wave DFB lasers modulated at MHz rates [2]. Such high-speed measurements yielded time-resolved temperature, pressure, and CO/CO_2 number densities in the exhaust of a rotating detonation rocket combustor over a range of conditions.

A critical factor in the aforementioned scanned-wavelength LAS methods is the spectral tuning rate. The maximum frequency tunability $\Delta\nu$ (also known as scan depth) achievable in our previous work was on the order of 0.5 cm^{-1} at 1 MHz (equivalent to $\Delta\lambda$ = 1.25 nm at 5 µm) [2]. At elevated gas pressures, spectral features broaden, and lines or features can become spectrally-unresolved by a laser a fixed scan depth. Thus, to deploy this sensor in higher pressure environments, it is desirable to have a larger scan depth. For multi-line temperature measurements using LAS, larger scan depth is also useful in capturing multiple spectral transitions with varying lower state energies with a single laser. In addition to the scan depth extension, it is further desirable to increase the signal-to-noise ratio (SNR) of these scanned-wavelength measurements to increase sensitivity, and although scanning typically adds consideration spectral information, injection current intensity modulation also typically implies that some of the measurement scan period involves low light intensity and thus low SNR.

In this work, we explore variations of modulation waveform to maximize scan depth and SNR for a distributed feedback quantum cascade laser in a bias-tee or RF-diplexed circuit with application to MHz-rate laser absorption measurements. The techniques include modulating the laser using rectangular/trapezoidal waveforms with prescribed ramp rates and comparing to sine waves. The influence of modulating below the current threshold is also explored, and limitations to the technique associated with the detection system bandwidth are evaluated. A waveform optimization is conducted based on common detector limitations to find a waveform that maximizes laser scan depth and SNR without exceeding detector bandwidth constraints, and demonstrated in a controlled detonation experiment for simultaneous measurement of temperature, pressure, and species.

III. Methodology

In this work, a continuous-wave distributed feedback (DFB) quantum cascade laser (QCL) (ALPES Lasers), tunable from 2002 to 2012 cm^{-1} is used as the target for scan depth maximization. Note that this *continuous-wave* laser must be differentiated from *pulsed* DFB lasers used by other groups for high-speed sensing [16], and typically offers better scan-to-scan repeatability. The laser temperature and mean injection current are set using an Arroyo 6310-QCL controller. A radio frequency (RF) signal is supplied by a digital function generator (Rigol DG1000Z) which can supply a maximum output frequency of 30 MHz. The function generator can output various waveforms: sine waves, square waves, as well as user-defined arbitrary waveforms. The DC current from the laser driver and the RF current from the function generator are diplexed using bias-tee circuitry to create an injection current waveform. A representative sinusoidal waveform is pictured at the top of Fig. 1.

To assess the laser output for a given injection current waveform, the laser beam is focused onto an AC-coupled MCT photovoltaic detector (Vigo PVI-4TE-6-1x1). The detector bandwidth spans between 10 Hz and 200 MHz. The detector output was collected at 1.25 GS/s using a Textronix MSO44 Oscilloscope with a 200 MHz bandwidth. A typical laser output trace is shown for a sinusoidal injection current waveform in the middle row of Fig. 1. To additionally assess the

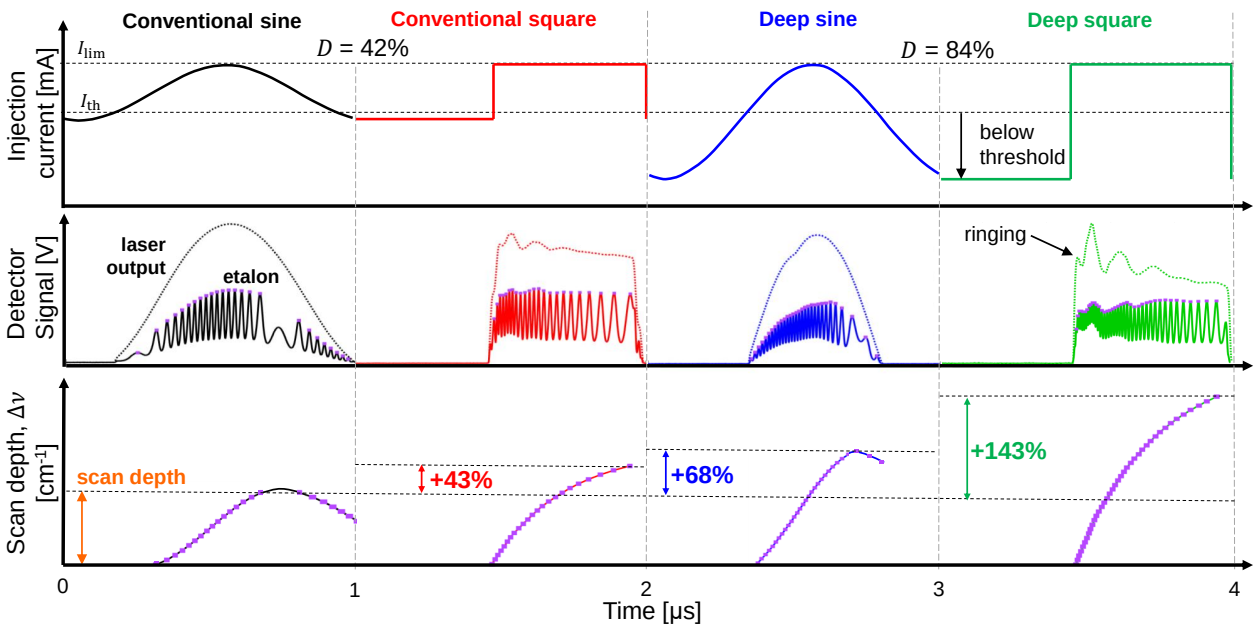

Fig. 1 ***Top*: Injection current *versus* time for various MHz waveforms. The conventional waveforms are modulated between the upper current limit and slightly below the lasing threshold, yielding a depth of modulation of 42%. The deep waveforms are modulated at a depth of 84%. *Middle*: detector signals produced by laser output (dotted curves) and signal when germanium etalon in beam path (solid curves). The successive peaks in the etalon signal correspond to a fixed change in laser wavelength. *Bottom*: Inferred laser scan depth *versus* time obtained from the etalon signal. The scan depth of the laser is indicated as the amplitude of the scan depth measurement and percent increases in scan depth are noted compared to the conventional sine wave.**

wavelength scanning of the laser, a 2-inch germanium etalon was placed into the beam path. The etalon's wavelength dependent transmissivity induces an oscillatory signal on the detector, which is also pictured in the middle row of Fig. 1. The etalon peaks are evenly spaced in the spectral domain by the etalon's free spectral range (FSR). By identifying the peak locations, the change in laser wavelength/frequency over time can be assessed. Two main regions can be identified. In the first one, the upscan, the laser wavelength is increasing as the laser chip is being heated by the injection current. In the second region, the downscan, the laser chip is being cooled and the wavelength is decreasing. Typically, the output intensity of the laser responds within nanoseconds to the injection current, and the laser temperature lags behind, yielding a corresponding lag in wavelength. A representative trace of laser wavelength versus time is shown at the bottom of Fig. 1. The amplitude of this wavelength modulation is identified as the scan depth of the laser modulation.

Since the bias-tee control method involves bypassing the laser driver, which provides safeguards and protections to the laser, a few additional steps and precautions must be taken when setting up the laser. Firstly, the function generator outputs a voltage signal whereas the laser accepts a current input. Thus, a transfer function H between the voltage amplitude of the function generator and the injection current amplitude to the laser must be established. This is done by first setting the DC current of the laser to some value I_{set} above the lasing threshold using the laser driver and then slowly increasing the amplitude of an RF sinusoidal waveform from the function generator. When the low end of the laser output intensity begins to flatten, the injection current is known to be reaching the lasing threshold current I_{th}. By using the known peak-to-peak voltage amplitude of the function generator output V_{pp}, the transfer function, H, can be determined:

$$H = \frac{2(I_{set} - I_{th})}{V_{pp}} \tag{1}$$

For the bias-tee laser system used in this work, the transfer function was approximately 14 mA/V. Knowledge of the transfer function enables the user to identify the actual minimum and maximum current values being applied to the laser for any given function generator output.

Additionally, for arbitrary waveforms, the average value of the input current is not necessarily equal to the average of the maximum and minimum output (V_{max} and V_{min}). As such, the offset of such waveforms should be adjusted such

that the cycle-averaged mean value of the output waveform is zero, to prevent unpredictable leakage of a DC (or low frequency) signal across the bias-tee. Failure to do so can cause laser overvoltage or reverse-biasing. Also, the DC current supplied by the laser driver should be set such that the maximum RF current I_{max} does not exceed the current limit of the laser I_{lim}. This condition can be met by ensuring the following condition:

$$I_{\text{set}} \leq I_{\text{lim}} - HV_{\text{max}} \tag{2}$$

In the same way, to prevent reverse-biasing the laser, the minimum injection current must be positive. This is ensured by ensuring the DC current satisfies the following condition:

$$I_{\text{set}} \geq HV_{\text{min}} \tag{3}$$

IV. Tuning and SNR Improvements

The mean temperature of the laser is typically set using thermoelectric cooling (TEC) of the laser controller. Temperature variation has the effect of changing the effective index of refraction of the waveguide, which shifts the output wavelength of the laser. In addition to the TEC, which sets a mean value, the laser temperature is modulated by the resistive or Ohmic heating from the injection current.

In our previous work [2], lasers were tuned with a sinusoidally varying injection current, which gradually changes the heating applied to the laser between a maximum and minimum value. By switching the waveform from a sine wave to a square wave, the laser heating no longer changes gradually. Instead, during the upscan, maximum current and heating are applied to the laser, and during the downscan, the maximum level of cooling is applied when the current is at its minimum value. These dramatic variations of heating and cooling allows the laser grating to reach greater extremes of temperature, resulting in higher scan depth. For the current setup, applying a conventional sine wave which is scanned between the lasing threshold (approximately 110 mA) and the maximum allowable current (190 mA), a scan depth of 0.40 cm^{-1} is achievable. With a square wave operating with the same current amplitude, a scan depth of 0.57 cm^{-1} is achievable, representing an increase of ~43%. The aforementioned sinusoidal and square waveforms are indicated in the first two columns of Fig. 1.

Beyond the increase in scan depth due to the waveform change, the signal-to-noise ratio (SNR) associated with the laser output increases with the square wave, as the laser ramps up to its maximum output power much more quickly and for longer in time than for a sine wave. Additionally, the SNR remains roughly constant across the scan, mitigating bias of the spectral measurement between regions of high and low SNR.

In addition to changing the waveform from a sine wave to a square wave, scan depth can also be extended by increasing the amplitude of the modulated current signal causing the injection current to drop far below the lasing threshold. This has the effect of increasing the intensity of the cooling which is applied to the laser when the injection current is at its minimum value. This enables the amplitude of the temperature change of the laser to increase even moreso, which improves the spectral scan depth despite the fact that the laser is not outputting light as it is scanned below the lasing threshold. We normalize the peak-to-peak current amplitude I_{pp} by the maximum current amplitude $I_{\text{pp,max}}$ (modulating from zero current to the current limit) to define a variable termed "depth of current modulation" D:

$$D = \frac{I_{\text{pp}}}{I_{\text{pp,max}}} = \frac{I_{\text{pp}}}{I_{\text{lim}}} \tag{4}$$

For the laser used in this work, scanning between the lasing threshold and current limit corresponds to a "threshold depth" of $D_{\text{th}} = 42\%$. To mitigate the risk of reverse-biasing the laser, a minimum current limit value was set as approximately 1/3 of the lasing threshold current, at 30 mA for this work, corresponding to a maximum depth of modulation of $D = 84\%$. The injection current profiles for these two values of depth are shown in Fig. 1, with the first two columns featuring waveforms at $D = 42\%$ and the second two columns featuring waveforms at $D = 84\%$.

The effect of the depth variation can be directly seen in Table 1. When the waveforms are modulated at the maximum depth of modulation, the scan depths increase to 0.67 cm^{-1} for the sine wave, and 0.97 cm^{-1} for the square wave. This represents a 68% and 143% increase respectively in scan depth compared to the conventional sine wave modulated at the threshold depth. The increase in depth can further be visualized in Fig. 1, where the deep sine and deep square are represented in the two rightmost columns.

Deep current modulation at high speeds allows for the laser to lase at temperatures that would otherwise be inaccessible. Typically, when the current applied to the laser decreases, the wavenumber output of the laser increases

Table 1 Variation of the scan-depth as a function of depth from 42% (conventional) to 84 % (deepest waveforms used in the work).

	Waveform	
Depth [%]	Sine wave	Square wave
42	0.40 cm^{-1}	0.57 cm^{-1}
84	0.67 cm^{-1}	0.97 cm^{-1}

(wavelength decreases) as the laser drops in temperature. When the current drops below the threshold current, the laser continues to cool, tuning the laser diffraction grating to higher wavenumbers. However, these frequencies of light are not outputted by the laser, as the laser power drops to zero below the lasing threshold. In the case of high-speed modulation, however, the lag between the laser intensity output and the laser temperature allows for the laser cavity to be tuned to a wavenumber associated with a "below-threshold" temperature while the power is ramped up above the threshold. By shifting the depth from $D = 42\%$ to $D = 84\%$ the spectral domain accessible by the laser was effectively extended by $\sim$1.5 cm^{-1}, which is equivalent in this case to shifting the laser TEC setpoint $\sim$10°C colder.

In addition to the variations in laser performance from waveform selection and depth of modulation, the effect of pulse duty cycle was also examined for the square wave. As the duty cycle is varied, there is a tradeoff between the amount of time spent heating and cooling the laser. For instance, a duty cycle above 50% involves longer periods of heating than cooling, and the opposite for a duty cycle below 50%. On the left side of Fig. 2 laser output intensity traces are shown for three square waves of varying duty cycle (20%, 50%, and 80%) which all share a depth of modulation of 84%. The achieved scan depth is maximized for a duty cycle of 50%, which agrees with observations made by Chrystie et al. for pulsed QCLs [16]. The variation of the scan depth with duty cycle can be seen with the black curve on the right side of Fig. 2.

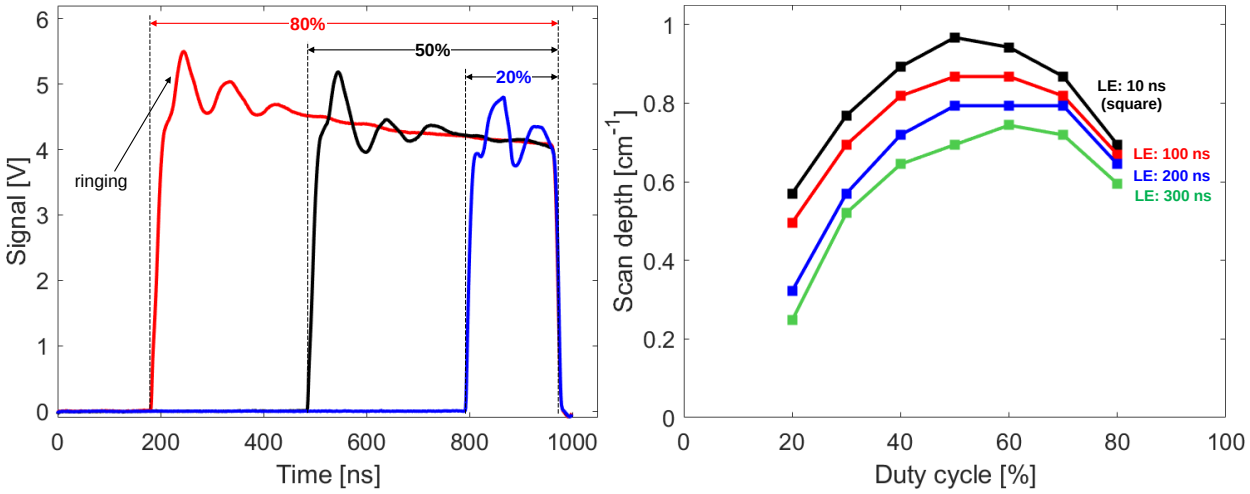

Fig. 2 *Left*: Detector signals for square waves with varying duty cycle. Ringing is noted at the beginning of the pulse and is further discussed in Section V. *Right*: Scan depth *versus* duty cycle for varying leading edge (LE) ramp times.

V. Detector bandwidth limitations

Extending the scan depth capability of DFB lasers can generate optical signals with high temporal frequency content. These high frequencies may come about due to 1) high-frequency oscillation of the laser output intensity or 2) high-frequency content generated by the absorption of light by a narrow spectral feature when making an absorption measurement through a gas.

The high-frequency oscillations in laser intensity appear as a "ringing" due to the overshoot in laser output power when the injection current under-goes a large step-change in current, on the order of nanoseconds [17, 18], and induced

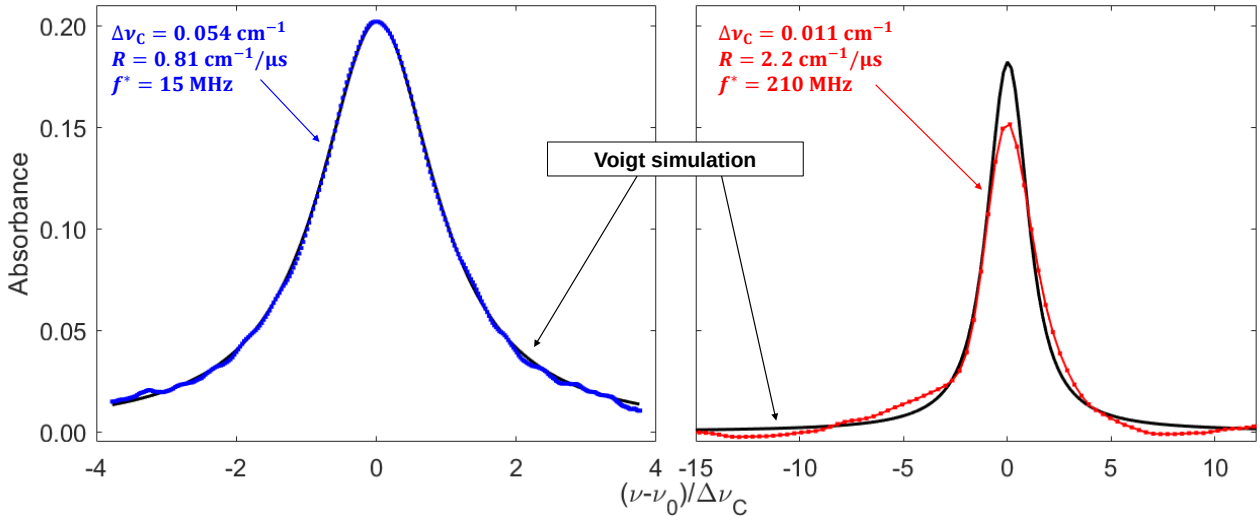

Fig. 3 ***Left*: Measurement of the $^{12}C^{16}O$ P(0,22) line at a low characteristic frequency in blue with simulated voigt profile in black. Close agreement is observed between measurement and simulation. *Right*: measurement of the same spectral feature at high characteristic frequency in red. This high-speed measurement features a reduced peak absorbance and artifacts associated with detector-induced signal distortion**

by the square waveform. Ringing can be observed at the beginning of the various square wave pulses shown on the left side of Fig. 2. The amplitude of ringing increases as the depth of current modulation is increased, since the laser current is changing more drastically. The high-frequency content in the optical signal due to laser ringing can exceed the rise time of the PV detector (related to the detector bandwidth) causing the signal to be distorted. The distortion of the laser signal by the detector prevents accurate measurement of the light intensity, which causes issues when the light intensity signal is used to make an absorbance measurement using the following equation:

$$\alpha = -\ln\left(\frac{I_t}{I_0}\right) \tag{5}$$

Here α is the absorbance, I_0 is the background light intensity without any absorbing gas present, and I_t is the transmitted light intensity when the laser beam is pitched through an absorbing medium. It is clear that if measurements of both I_0 and I_t have high frequency content filtered out, the absorption measurement will be distorted. An example of such a distorted absorbance measurement is shown in Fig. 3.

Even if the background light intensity itself has low frequency content (as is the case for a sinusoidal laser output), the transmitted light intensity I_t can have high frequency content due to the presence of narrow spectral features that absorb light. These spectral features can cause rapid changes in laser intensity as the laser wavelength rapidly changes. This type of distortion will only occur when either the spectral features have a narrow linewidth or when the rate of change of the laser output frequency is high. We term the rate of change of the frequency output of the laser as the "chirp rate" R [16]:

$$R = \frac{d\nu}{dt} \tag{6}$$

For mid-infrared spectra of gaseous species relevant to combustion (i.e. CO, CO_2, H_2O) at pressures near or above atmospheric, the dominant contributor to the linewidth is collisional broadening which scales linearly with gas pressure. As such, the bandwidth related distortion will be pronounced at lower pressures. From previous work, the minimum pressure observed at the exhaust of a rotating detonation engine was on the order of 0.5 atm, so we set this as a minimum target pressure in this work.

It is postulated that for a given detector bandwidth, there will be a maximum "characteristic frequency" f^* associated with the light intensity oscillation due to the narrow spectral feature:

$$f^* = \frac{R}{\Delta\nu_C} \tag{7}$$

Equivalently, a "characteristic time" τ^* may be defined, which intuitively represents the time corresponding to the full-width half maximum (FWHM) of the spectral feature:

$$\tau^* = \frac{1}{f^*} = \frac{\Delta\nu_C}{R} \tag{8}$$

In order to identify the maximum allowable characteristic frequency for the target line used in this work (with ~200 MHz bandwidth detection system), a series of measurements of room temperature CO were conducted by placing a 33.94-cm static gas cell into the optical path. This gas cell was filled with pure CO to various fill pressures. Before the cell was filled, a measurement of the background intensity was taken, and a measurement was taken with the etalon in the beam path, to aid in transforming the results from the time domain to the spectral frequency domain. After the cell was filled, the transmitted light intensity was recorded, and an absorbance measurement was calculated using Eqn. 5.

The laser's center wavelength was tuned to the P(0,22) line of $^{12}C^{18}O$, which was selected due to its isolation from other CO lines and from spectra of ambient water. Measurements were performed using sine waves in order to isolate the effects of high-frequency absorption signals from the ringing observed using square waves. The chirp rate of these sine waves were adjusted by varying the depth of modulation and the laser modulation frequency. In addition, the characteristic frequency of the measurement is adjusted by filling the gas cell to different pressures, resulting in variation in the linewidth of the spectral feature.

Sample room temperature absorbance measurements are shown in Fig. 3. A range of characteristic frequency measurements were collected spanning from 10 MHz to 400 MHz. At low characteristic frequencies, the measured absorbance spectra agrees closely with simulated spectra using linestrength and broadening parameters from HITRAN 2020 [19], as indicated on the left side of Fig. 3. At high characterstic frequencies the measured lineshape becomes distorted, as indicated in Fig. 3. There is a reduction in the measured peak absorbance, along with signal artifacts in the wings of the line. This distortion precludes accurate fitting of the absorption lineshape.

In order to assess the magnitude of the detector induced distortion on the measured lineshape, a nonlinear least squares fitting routine was conducted on the measured absorbance spectra. In this fitting routine, the collision linewidth, absorbance area, and absolute line position of the line were allowed to float. The three parameters were varied until a solution minimizing the sum of squared errors between the measurement and fit was found. The error in fitted collision linewidth and absorbance area is plotted in Fig. 4 against the characteristic frequency of the absorption measurement. It can be seen that for lower characteristic frequencies, the error in the measured spectral parameters is low and on the order of the scan to scan variation in the error, as indicated by the vertical error bars. At higher frequencies however, the

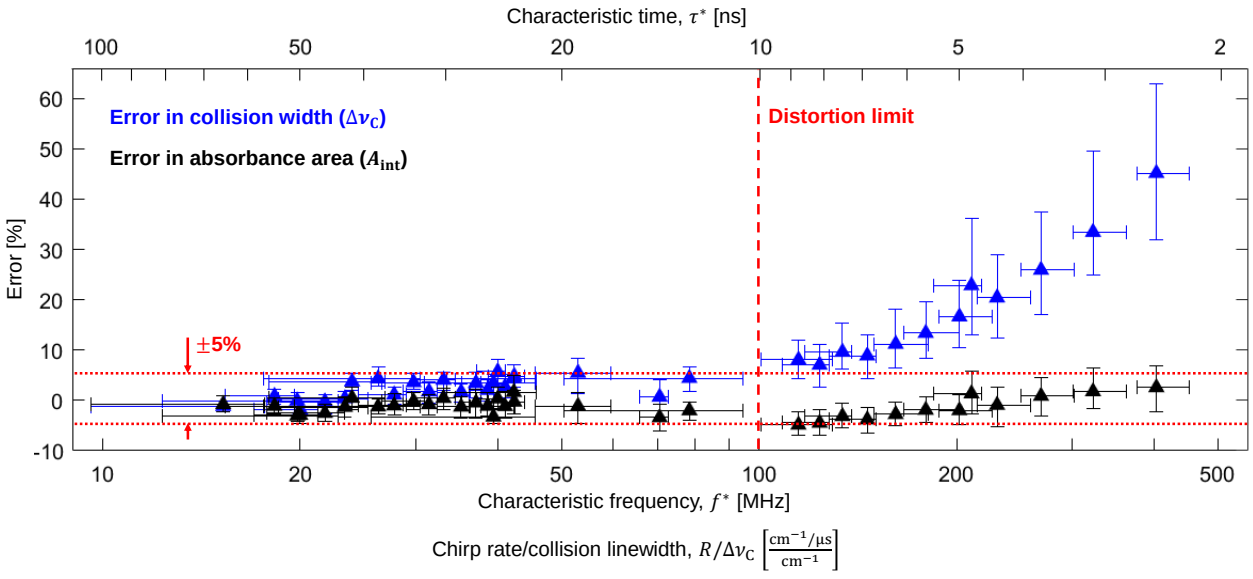

Fig. 4 Error in fitted collision width and absorbance area of the $^{12}C^{18}O$ P(0,22) line at various characteristic frequencies (chirp rate over linewidth). The error in the fit of $\Delta\nu_C$ is seen to increase significantly past $f^* = 100$ MHz

fitted collision width ends up being higher than the true collision width, resulting in an instrument induced broadening of the line. It is interesting to note that the fitted absorbance area is more robust to the detector induced distortion, with the error in the fitted areas staying within ±5% even at the highest characteristic frequencies.

The critical characteristic frequency beyond which the collisional linewidth measurement error exceeds 5% is approximately 100 MHz, exactly 1/2 the detection system bandwidth f_{BW} = 200 MHz, implying that the following criteria must be met to mitigate detector induced distortion of absorption signals:

$$f^* < \frac{1}{2} f_{\mathrm{BW}} \tag{9}$$

We can use the above criteria to establish a maximum laser chirp rate using a given detection system bandwidth for measurement of a given spectral feature. For example, if the $^{12}C^{16}O$ P(0,22) line was to be measured down to pressures of 0.5 atm ($\Delta\nu_C$ = 0.053 cm^{-1}) using a 200 MHz bandwidth detection system, a measurement with a 5% accuracy imposes a maximum chirp rate of 5.3 cm^{-1}/μs. We apply a conservative factor of 2 to this limit, and therefore set R_{max} = 2.65 cm^{-1}/μs. With knowledge of such a limit, the waveforms discussed in Section IV can be re-evaluated. Some of these waveforms resulted in chirp rates that exceeded this limit during some portion of the scan. We can define a usable spectral scan depth, $\Delta\nu_{\mathrm{use}}$, which corresponds to the spectral scan depth, $\Delta\nu$, restricted to the portion of the scan where the chirp rate is below R_{max}:

$$\Delta\nu_{\mathrm{use}} = \Delta\nu\big|_{R<R_{\mathrm{max}}} \tag{10}$$

For the conventional sine wave (D = 42%), the deep sine wave (D = 84%), and the conventional square wave (D = 42%), the chirp rate never exceeds the maximum allowable value. Thus, their usable scan depths are equal to the actual scan depths. However, for the deep square waves, the chirp rate does exceed the limiting value at the beginning of the upscan, meaning that spectral features positioned at the beginning of the scan could be potentially distorted. The usable scan depth for the deep square is therefore reduced from 0.97 cm^{-1} to 0.45 cm^{-1}, rendering it less useful than the conventional square wave, deep sine, and even the conventional sine. In fact, when considering usable scan depth, maximizing D does not maximize $\Delta\nu_{\mathrm{use}}$. For a square wave, the usable scan depth is roughly similar for depth values between 40 and 65%, yielding an approximate usable scan depth of 0.57 cm^{-1}. The scan depths versus time for the aforementioned waveforms are indicated in Fig. 5. A dashed line is plotted indicating the slope corresponding to the maximum chirp rate, which the extended square clearly exceeds. In the next section, we will show that an optimal compromise between the extended sine and the extended square can be found using arbitrary waveform generation.

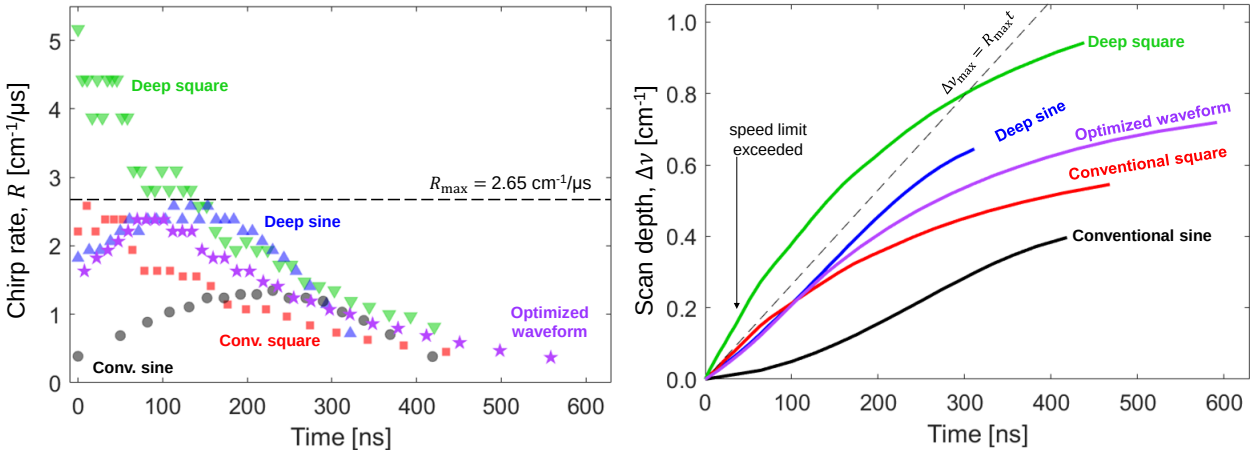

Fig. 5 ***Left*: Chirp rate *versus* time for the conventional sine, conventional square, deep sine, deep square, and optimized waveform. The deep square is observed to exceed the chirp rate limit of 2.65 cm^{-1}. *Right*: Scan depth *versus* time for the same waveforms. The extended square yields the highest scan depth but exceeds the detector limited chirp rate. The optimized waveform achieves high scan depth while remaining below the speed limit.**

VI. Waveform optimization

To mitigate the issues associated with detector bandwidth, it is desirable to slow the initial rate of change of the laser output power and output frequency. To accomplish this, a linear ramp in current can be added to the beginning of the pulse, turning the square to a trapezoid. This ramp has the effect of providing more gradual heating to the laser, resulting in slower wavelength tuning and also mitigates ringing in the optical output signal. These effects can be seen in the left and middle columns Fig. 6 where 50% duty cycle pulses with leading edge lengths of 10 ns and 300 ns are compared.

As the length of the leading edge ramp is increased, the overall scan depth achieved by the laser is necessarily reduced, along with a reduction in SNR during the initial part of the scan. Despite this, the usable scan depth increases. For the 50% duty cycle waveform, shifting from a 10 ns ramp to a 300 ns ramp boosts the usable scan depth from 0.45 cm^{-1} to 0.50 cm^{-1}. Additionally, as the length of the leading edge ramp is increased the optimal duty cycle for maximizing scan depth shifts to higher values than 50% to compensate for the less efficient heating compared to cooling. This effect can be seen on the right side of Fig. 2.

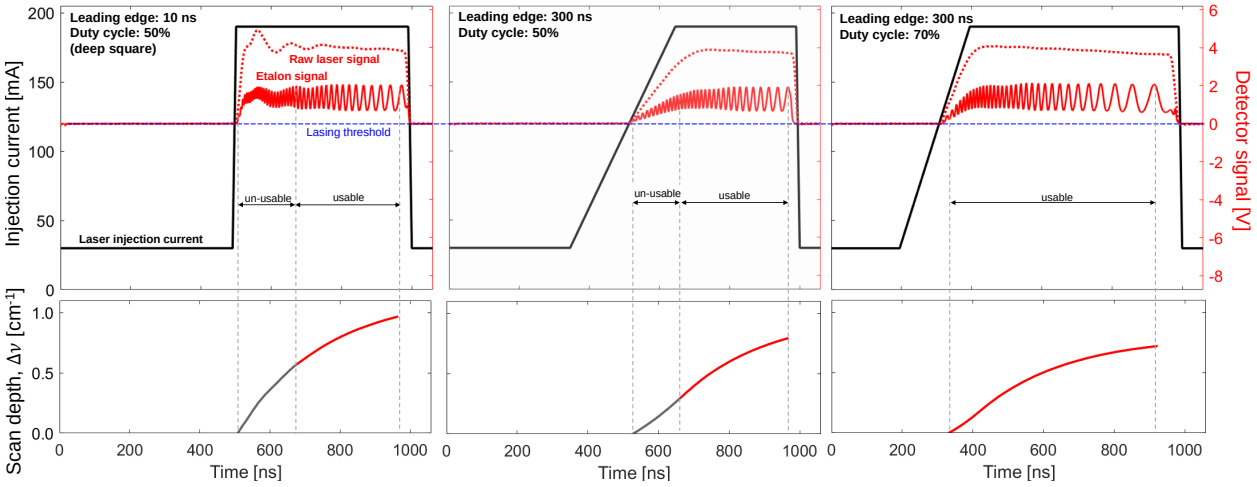

Fig. 6 ***Top*: Laser injection current and detector signals for a 50 % duty cycle trapezoidal waveform with a 10 ns leading edge (left) and a 300 ns leading edge (middle). The addition of the ramp reduces the ringing in the detector signal and reduces the chirp rate of the laser, improving usable scan depth. The optimized waveform with a 300 ns ramp and 70% duty cycle is shown on the right. The combined effect of the leading edge ramp and increased duty cycle keep the chirp rate below the detector limit, making the entire scan usable.**

In order to find a trapezoidal waveform that maximizes scan depth while also $R_{max} < 2.65$ cm^{-1}, a multi-parameter optimization was conducted in which the leading edge ramp time, duty cycle, and depth of modulation are varied. Laser output intensity and etalon signal were recorded for the various trapezoidal waveforms and the scan depth and maximum chirp rate were identified for each waveform. The waveform with the highest usable scan depth was selected as the optimized waveform after verifying visually that the laser output intensity did not display significant ringing. The selected waveform had a depth of modulation of 84%, a duty cycle of 70%, and a leading edge ramp time of 300 ns, with a usable scan depth of 0.7 cm^{-1}. The injection current profile, laser output intensity, etalon signal, and output frequency versus time are shown in Fig. 6. It can be clearly seen that this waveform does not induce ringing in the laser power output.

To validate that no distortion of the absorbance signal was occurring, room temperature measurements similar to those described in Section V were conducted. For each measurement, the gas cell was filled to 0.5 atm with pure CO. Between each test, the laser TEC setpoint was tuned to reposition the spectral feature at various positions along the scan. For all tests, the error in measured collision linewidth was less than ±5%, validating the lack of detector induced distortion.

The key constraint in the optimization is the maximum allowable chirp rate. This maximum chirp rate is obtained using Eqns. 7 and 10 based on the detection system bandwidth and the linewidth of the target spectral features. The maximum allowable chirp rate can be increased by using a higher bandwidth detection system or by targeting broader spectral features. By tuning these two parameters, other waveforms with larger scan depths can be employed.

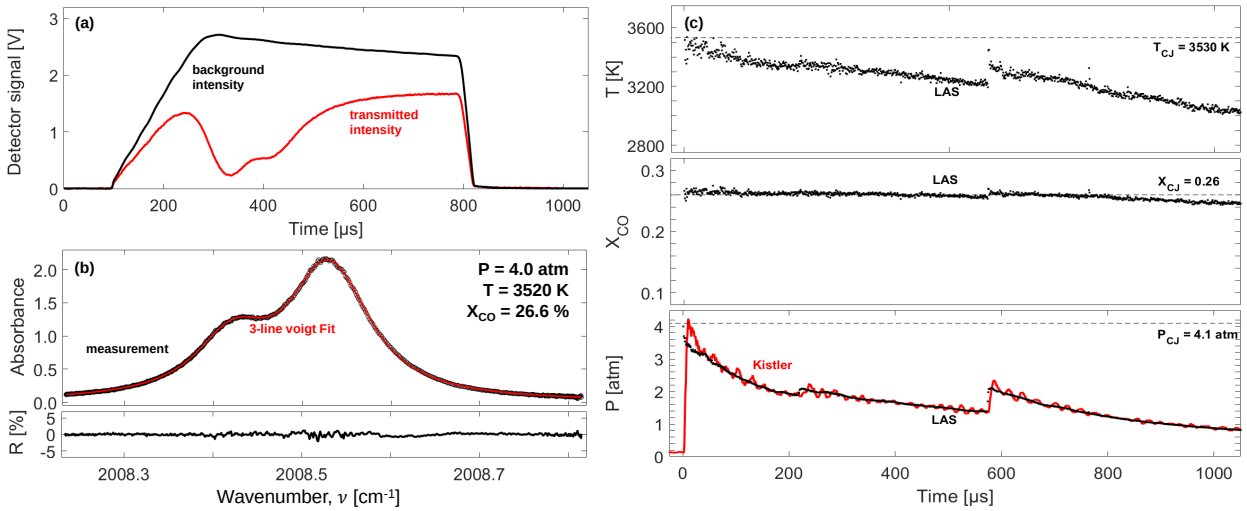

Fig. 7 (a) Detector measured background and transmitted intensity signals. The transmitted intensity is measured 1 μs after the detonation wave passes the measurement location. The absorption of light by CO is clearly visible. (b) Measured absorbance in black along with a three-line voigt fit in red. Residuals on the order of ±2% are pictured below in black. (c) Time histories of temperature, CO mole fraction and pressure obtained using LAS over the course of the detonation experiment. The measured properties are compared to the values computed using CJ detonation theory. The pressure measurement is additionally compared to a mechanical pressure measurement using a Kistler pressure transducer.

VII. Demonstration

To demonstrate the utility of the optimized waveform described in the previous section for MHz-rate measurements, experiments were conducted on UCLA's Detonation Impulse Tube (DIT) facility [12]. In these experiments a mixture of stoichiometric ethylene (C_2H_4) and oxygen (O_2) were spark ignited at one end of a 6 ft long 1.5" ID tube with a Schelkin Spiral to aid in deflagration-to-detonation transition. The flame produced by this ignition event transitioned to a detonation wave, as confirmed via wave speed measurements made by piezoelectric sensors located near the end of the tube. The wave speeds were seen to match (within measurement uncertainty) values predicted for an ideal 1-dimensional Chapman-Jouguet detonation wave, as predictued using CalTech's Shock Detonation Toolbox [20] in CANTERA [21] using the GRI-MECH 3.0 mechanism [22]. During these experiments the light emitted from the laser discussed in the previous sections is pitched through the detonation tube via two wedged sapphire windows providing optical access. The laser was tuned to target the P(0,31), P(2,20), and P(3,14) rovibrational transitions of CO and pressure, temperature, and concentration of CO are measured using the measured spectra as in [2]. A sample absorption measurement is shown in the top left of Fig. 7 representing a time 1 μs after the passage of the detonation wave, when CO is first observed at the measurement location. A fit of the measured spectra is pictured below, which was used to find the following gas properties: $P = 4.0$ atm, $T = 3520$ K, and $X_{CO} = 26.6\%$. The residuals between the fit and measurement are generally below ±2%.

The time histories of the measured gas properties are shown on the right side of Fig. 7, with each property being measured at 1 MHz and without any averaging. The low scatter in the measured properties is a result of the high signal-to-noise ratio, spectral resolution, and scan-to-scan stability of the CW laser and the selected injection current waveform. The measured properties can be compared to values predicted by the Chapman-Jouguet theory obtained using the aforementioned Shock and Detonation Toolbox. These values are indicated as horizontal dashed lines in Fig. 7. The measurement also captures decay in temperature and pressure from their CJ values after the initial passage of the detonation wave, associated with the Taylor expansion wave [23]. Additionally, the measurement captures the effect of reflected pressure waves resulting from the impact of the detonation wave on the plastic diaphragm located at the end of the tube. These reflected waves result in an increase in temperature and pressure at the measurement location. The mole fraction of CO is relatively constant (at the CJ-predicted value) in the post-detonation region, with a small rise observed during the passage of the reflected wave and a slight decay noted towards the end of the test, as the gas temperature drops.

The LAS pressure measurement is particularly advantageous due to the dynamic nature of the pressure trace. The Kistler measurement, which has an effective measurement bandwidth of 100 kHz, is prone to ringing and overshoot due to the impulse response of the mechanical sensor to step changes in pressure. The LAS pressure measurement is immune to this mechanical overshoot. Additionally, the Kistler measurement is slower to respond to changes in pressure than the LAS measurement, with the rise in Kistler pressure lagging the pressure rise observed in the LAS measurement by approximately 3 µs.

VIII. Summary

Techniques for extending the spectral tuning range and signal-to-noise ratio for MHz-rate scanned-wavelength laser absorption spectroscopy were explored with cw-DFB lasers in a bias-tee circuit. Laser chirp rates are increased by modulating the laser using square waves instead of sine waves and by scanning the laser below the lasing threshold, yielding scan depths on the order of 1 cm^{-1} at 1 MHz. The effect of square waveform duty cycle and leading edge are examined. The attenuation of the high-frequency laser signals due to detector bandwidth are also examined, and limitations are noted. Based on common detector limitations, an optimized waveform is established for a 200-MHz bandwidth detection system. This waveform is validated using room temperature laser absorption measurements. The waveform is then deployed for use in a detonation tube to measure temperature, pressure, and CO concentration at MHz rates behind a detonation wave.

Acknowledgements

This work was supported by the Air Force Research Laboratory (AFRL) and OptoKnowledge Systems Inc. under a Small Business Technology Transfer (STTR) program, award no. FA9300-19-P-1503 with Dr. John W. Bennewitz as contract monitor, and Dr. Jason Kriesel as collaborator. Supplementary support was provided by the U.S. National Science Foundation (NSF), award no. 1752516 and the Air Force Office of Scientific Research (AFOSR) Young Investigator Program (YIP) award no. FA9550-19-1-0062 with Dr. Chiping Li as Program Officer. Nicolas Q. Minesi acknowledges support from NASA's Space Technology Research Grants Program (award no. 80NSSC21K0066). Christopher C. Jelloian is supported by a NASA Space Technology Research Fellowship.

References

[1] Mathews, G. C., Blaisdell, M. G., Lemcherfi, A. I., Slabaugh, C. D., and Goldenstein, C. S., "High-bandwidth absorption-spectroscopy measurements of temperature, pressure, CO, and H 2 O in the annulus of a rotating detonation rocket engine," *Applied Physics B: Lasers and Optics*, Vol. 127, No. 12, 2021, pp. 1–23. https://doi.org/10.1007/s00340-021-07703-9, URL https://doi.org/10.1007/s00340-021-07703-9.

[2] Nair, A. P., Lee, D. D., Pineda, D. I., Kriesel, J., Hargus, W. A., Bennewitz, J. W., Danczyk, S. A., and Spearrin, R. M., "MHz laser absorption spectroscopy via diplexed RF modulation for pressure, temperature, and species in rotating detonation rocket flows," *Applied Physics B*, Vol. 126, No. 8, 2020, p. 138. https://doi.org/10.1007/s00340-020-07483-8, URL https://link.springer.com/10.1007/s00340-020-07483-8.

[3] Peng, W. Y., Cassady, S. J., Strand, C. L., Goldenstein, C. S., Spearrin, R. M., Brophy, C. M., Jeffries, J. B., and Hanson, R. K., "Single-ended mid-infrared laser-absorption sensor for time-resolved measurements of water concentration and temperature within the annulus of a rotating detonation engine," *Proceedings of the Combustion Institute*, Vol. 37, No. 2, 2019, pp. 1435–1443. https://doi.org/10.1016/j.proci.2018.05.021.

[4] Goldenstein, C. S., Spearrin, R. M., Jeffries, J. B., and Hanson, R. K., "Infrared laser absorption sensors for multiple performance parameters in a detonation combustor," *Proceedings of the Combustion Institute*, Vol. 35, No. 3, 2015, pp. 3739–3747. https://doi.org/10.1016/j.proci.2014.05.027.

[5] Spearrin, R. M., Goldenstein, C. S., Jeffries, J. B., and Hanson, R. K., "Quantum cascade laser absorption sensor for carbon monoxide in high-pressure gases using wavelength modulation spectroscopy," *Applied Optics*, Vol. 53, No. 9, 2014, p. 1938. https://doi.org/10.1364/AO.53.001938.

[6] Spearrin, R. M., Goldenstein, C. S., Jeffries, J. B., and Hanson, R. K., "Mid-infrared Laser Absorption Diagnostics for Detonation Studies," *29th International Symposium on Shock Waves 1*, Springer International Publishing, Cham, 2015, pp. 259–264. https://doi.org/10.1007/978-3-319-16835-7{_}39.

[7] Sanders, S. T., Baldwin, J. A., Jenkins, T. P., Baer, D. S., and Hanson, R. K., "Diode-laser sensor for monitoring multiple combustion parameters in pulse detonation engines," *Proceedings of the Combustion Institute*, Vol. 28, No. 1, 2000, pp. 587–594. https://doi.org/10.1016/s0082-0784(00)80258-1.

[8] Caswell, A. W., Roy, S., An, X., Sanders, S. T., Schauer, F. R., and Gord, J. R., "Measurements of multiple gas parameters in a pulsed-detonation combustor using timedivision-multiplexed Fourier-domain mode-locked lasers," *Applied Optics*, Vol. 52, No. 12, 2013, pp. 2893–2904. https://doi.org/10.1364/AO.52.002893.

[9] Ma, L., Sanders, S. T., Jeffries, J. B., and Hanson, R. K., "Monitoring and control of a pulse detonation engine using a diode-laser fuel concentration and temperature sensor," *Proceedings of the Combustion Institute*, Vol. 29, No. 1, 2002, pp. 161–166. https://doi.org/10.1016/S1540-7489(02)80025-6.

[10] Klingbeil, A. E., Jeffries, J. B., and Hanson, R. K., "Design of a fiber-coupled mid-infrared fuel sensor for pulse detonation engines," *AIAA Journal*, Vol. 45, No. 4, 2007, pp. 772–778. https://doi.org/10.2514/1.26504.

[11] Goldenstein, C. S., Spearrin, R. M., Jeffries, J. B., and Hanson, R. K., "Infrared laser-absorption sensing for combustion gases," *Progress in Energy and Combustion Science*, Vol. 60, 2017, pp. 132–176. https://doi.org/10.1016/j.pecs.2016.12.002.

[12] Nair, A. P., Jelloian, C., Morrow, D. S., Bendana, F. A., Pineda, D. I., and Spearrin, R. M., "MHz mid-infrared laser absorption sensor for carbon monoxide and temperature behind detonation waves," *AIAA Scitech 2020 Forum*, American Institute of Aeronautics and Astronautics, 2020, pp. 2021–0448. https://doi.org/10.2514/6.2020-0733, URL https://arc.aiaa.org/doi/10.2514/6.2020-0733.

[13] Nair, A. P., Lee, D., Pineda, D., Spearrin, R. M., Krisel, J., Hargus, W. A., Bennewitz, J. W., and Danczyk, S., "MHz Mid-infrared Laser Absorption of CO and CO 2 for Pressure, Temperature, and Species in Rotating Detonation Rocket Flows," *AIAA Propulsion and Energy 2020 Forum*, American Institute of Aeronautics and Astronautics, 2020. https://doi.org/10.2514/6.2020-3867.

[14] Nair, A. P., Lee, D. D., Pineda, D. I., Kriesel, J., Hargus, W. A., Bennewitz, J. W., Bigler, B., Danczyk, S. A., and Spearrin, R. M., "Methane-Oxygen Rotating Detonation Exhaust Thermodynamics with Variable Mixing, Equivalence Ratio, and Mass Flux," *Aerospace Science and Technology*, Vol. 113, 2021, p. 106683. https://doi.org/10.1016/j.ast.2021.106683.

[15] Jelloian, C. C., Bendana, F. A., Wei, C., Spearrin, R. M., and MacDonald, M. E., "Non-equilibrium vibrational, rotational, and translational thermometry via MHz laser absorption of CO," *Journal of Thermophysics and Heat Transfer*, 2021. https://doi.org/https://doi.org/10.2514/1.T6376.

[16] Chrystie, R. S., Nasir, E. F., and Farooq, A., "Towards simultaneous calibration-free and ultra-fast sensing of temperature and species in the intrapulse mode," *Proceedings of the Combustion Institute*, Vol. 35, No. 3, 2015, pp. 3757–3764. https://doi.org/10.1016/j.proci.2014.06.069, URL http://dx.doi.org/10.1016/j.proci.2014.06.069https://linkinghub.elsevier.com/retrieve/pii/S1540748914002272.

[17] Ohtsubo, J., *Semiconductor lasers and theory*, 1977. https://doi.org/10.1007/978-3-319-56138-7{_}3.

[18] Jin, X., and Chuang, S. L., "High-speed modulation of semiconductor lasers," *IEEI Transactions on Electron Devices*, Vol. 32, No. 12, 1985, pp. 2572–2584. https://doi.org/10.1364/ofc.1984.mj1.

[19] Gordon, I., Rothman, L., Hargreaves, R., Hashemi, R., Karlovets, E., Skinner, F., Conway, E., Hill, C., Kochanov, R., Tan, Y., Wcisło, P., Finenko, A., Nelson, K., Bernath, P., Birk, M., Boudon, V., Campargue, A., Chance, K., Coustenis, A., Drouin, B., Flaud, J., Gamache, R., Hodges, J., Jacquemart, D., Mlawer, E., Nikitin, A., Perevalov, V., Rotger, M., Tennyson, J., Toon, G., Tran, H., Tyuterev, V., Adkins, E., Baker, A., Barbe, A., Canè, E., Császár, A., Dudaryonok, A., Egorov, O., Fleisher, A., Fleurbaey, H., Foltynowicz, A., Furtenbacher, T., Harrison, J., Hartmann, J., Horneman, V., Huang, X., Karman, T., Karns, J., Kassi, S., Kleiner, I., Kofman, V., Kwabia–Tchana, F., Lavrentieva, N., Lee, T., Long, D., Lukashevskaya, A., Lyulin, O., Makhnev, V., Matt, W., Massie, S., Melosso, M., Mikhailenko, S., Mondelain, D., Müller, H., Naumenko, O., Perrin, A., Polyansky, O., Raddaoui, E., Raston, P., Reed, Z., Rey, M., Richard, C., Tóbiás, R., Sadiek, I., Schwenke, D., Starikova, E., Sung, K., Tamassia, F., Tashkun, S., Vander Auwera, J., Vasilenko, I., Vigasin, A., Villanueva, G., Vispoel, B., Wagner, G., Yachmenev, A., and Yurchenko, S., "The HITRAN2020 molecular spectroscopic database," *Journal of Quantitative Spectroscopy and Radiative Transfer*, Vol. 277, 2022, p. 107949. https://doi.org/10.1016/j.jqsrt.2021.107949.

[20] Browne, S., Ziegler, J., and Shepherd, J. E., "Numerical Solution Methods for Shock and Detonation Jump Conditions," *GALCIT Report FM2006.006*, 2004.

[21] Goodwin, D. G., Moffat, H. K., and Speth, R. L., "Cantera: An object-oriented software toolkit for chemical kinetics, thermodynamics, and transport processes," , 2018. https://doi.org/10.5281/zenodo.170284.

[22] Smith, G. P., Golden, D. M., Frenklach, M., Moriarty, N. W., Eiteneer, B., Goldenberg, M., Bowman, C. T., Hanson, R. K., Song, S., Gardiner, W. C., Lissianski, V. V., and Qin, Z., "GRI-MECH 3.0," , 1999. URL http://www.me.berkeley.edu/gri_mech/.

[23] "The dynamics of the combustion products behind plane and spherical detonation fronts in explosives," *Proceedings of the Royal Society of London. Series A. Mathematical and Physical Sciences*, Vol. 200, No. 1061, 1950, pp. 235–247. https://doi.org/10.1098/rspa.1950.0014.